AGU PUBLICATIONS

JGR

Journal of Geophysical Research: Space Physics

RESEARCH ARTICLE
10.1002/2016JA022817

Key Points:
- Lower atmospheric forcing has a significant impact on *Sq* variability
- Atmospheric tides play a role in driving *Sq* variability
- The *Dst* index is partly due to ionospheric currents

Correspondence to:
Y. Yamazaki,
y.yamazaki@lancaster.ac.uk

Citation:
Yamazaki, Y., K. Häusler, and J. A. Wild (2016), Day-to-day variability of midlatitude ionospheric currents due to magnetospheric and lower atmospheric forcing, *J. Geophys. Res. Space Physics*, *121*, 7067–7086, doi:10.1002/2016JA022817.

Received 15 APR 2016
Accepted 30 JUN 2016
Accepted article online 5 JUL 2016
Published online 23 JUL 2016

Day-to-day variability of midlatitude ionospheric currents due to magnetospheric and lower atmospheric forcing

Y. Yamazaki[1], K. Häusler[2], and J. A. Wild[1]

[1]Department of Physics, Lancaster University, Lancaster, UK, [2]High Altitude Observatory, National Center for Atmospheric Research, Boulder, Colorado, USA

Abstract As known from previous studies on the solar quiet (*Sq*) variation of the geomagnetic field, the strength and pattern of ionospheric dynamo currents change significantly from day to day. The present study investigates the relative importance of two sources that contribute to the day-to-day variability of the ionospheric currents at middle and low latitudes. One is high-latitude electric fields that are caused by magnetospheric convection, and the other is atmospheric waves from the lower atmosphere. Global ionospheric current systems, commonly known as *Sq* current systems, are simulated using the National Center for Atmospheric Research thermosphere-ionosphere-mesosphere-electrodynamics general circulation model. Simulations are run for 1–30 April 2010 with a constant solar energy input but with various combinations of high-latitude forcing and lower atmospheric forcing. The model well reproduces geomagnetic perturbations on the ground, when both forcings are taken into account. The contribution of high-latitude forcing to the total *Sq* current intensity (J_{total}) is generally smaller than the contribution of wave forcing from below 30 km, except during active periods ($Kp \geq 4$), when J_{total} is enhanced due to the leakage of high-latitude electric fields to lower latitudes. It is found that the penetration electric field drives ionospheric currents at middle and low latitudes not only on the dayside but also on the nightside, which has an appreciable effect on the *Dst* index. It is also found that quiet time day-to-day variability in J_{total} is dominated by symmetric-mode migrating diurnal and semidiurnal tidal winds at 45–60° latitude at ~110 km.

1. Introduction

Electrodynamics of the middle- and low-latitude ionosphere are dominated by the wind dynamo mechanism, in which electric fields and currents are generated by the action of neutral winds [e.g., *Richmond*, 1995a; *Vasyliūnas*, 2012]. The topic has been important not only for the understanding of the ionosphere but also for accurate modeling of the Earth's magnetic field because ionospheric currents are a significant source of geomagnetic field perturbations [e.g., *Sabaka et al.*, 2002; *Chulliat et al.*, 2013]. For the time scale longer than a minute, the ionospheric electrodynamics can be considered to be steady state. In this case, the electric current density **J** can be expressed using ionospheric Ohm's law as follows:

$$\mathbf{J} = \hat{\sigma} \cdot (\mathbf{E} + \mathbf{U} \times \mathbf{B}) \tag{1}$$

where $\hat{\sigma}$ is the ionospheric conductivity tensor, **E** is electric field, **U** is neutral wind, and **B** is the main geomagnetic field. The horizontal currents flow mostly in the daytime ionosphere within the altitude range 90–150 km where the ionospheric conductivity is large; this region is often called the dynamo region. During geomagnetically quiet periods, the dynamo region currents produce regular daily variations of the geomagnetic field (of the order of tens of nanoteslas), commonly known as solar quiet (*Sq*) variations [e.g., *Campbell*, 1989]. For this reason, the dynamo region currents are often referred to as *Sq* currents.

The strength and pattern of *Sq* currents change on various time scales with $\hat{\sigma}$, **E**, **U**, and **B**. The conductivity of the ionosphere strongly depends on the plasma density and thus varies with solar activity. The resulting solar cycle variation dominates long-term (year-to-year) variability of the *Sq* currents [e.g., *Campbell and Matsushita*, 1982; *Takeda*, 2002, 2013]. Previous studies have also recognized significant short-term (hour-to-hour and day-to-day) variability in the *Sq* currents [e.g., *Hasegawa*, 1960; *Suzuki*, 1978, 1979; *Briggs*, 1984; *Takeda*, 1984]. The day-to-day variation of *Sq* is often "random-like," and the driving mechanism is not well understood.

Since much of the day-to-day variation occurs without a corresponding change in solar activity, sources other than solar radiation forcing must be taken into account.

Neutral winds are often thought to be responsible for the short-term variability of *Sq*. In the dynamo region, atmospheric tides dominate the global wind field. These tides are generated in the stratosphere by absorption of solar radiation by ozone and in the troposphere by absorption of infrared radiation and latent heat release [e.g., *Zhang et al.*, 2010a, 2010b, and references therein]. As the tidal waves propagate upward from the source regions, they grow exponentially with height, and at dynamo region altitudes, they attain amplitudes of several tens of meters per second in the horizontal wind. While tides propagate through the middle atmosphere, they interact with the mean flow and with other atmospheric waves and tides. All these interactions affect the amplitude and phase of the tides that reach the dynamo region. Consequently, tides in the dynamo region show significant short-term variability [e.g., *Liu*, 2014]. *Miyahara and Ooishi* [1997] examined the impact of variable neutral winds on the ionospheric wind dynamo on the basis of a thin-shell dynamo model with winds obtained from a general circulation model of the middle atmosphere. They showed that wave forcing in the dynamo region from below makes a significant contribution to the day-to-day variability of the dynamo region currents and ground-level *Sq* variations. More recent work, using more realistic dynamo models and winds, has also highlighted the importance of lower atmospheric forcing for the short-term variability of ionospheric electrodynamics [*Kawano-Sasaki and Miyahara*, 2008; *Jin et al.*, 2011; *Liu et al.*, 2013; *Fang et al.*, 2013; *Yamazaki et al.*, 2014a].

Although the numerical studies mentioned above successfully reproduced realistically large electrodynamic variability by taking into account the effect of variable neutral winds, it is possible that other mechanisms also play a key role. In particular, the present study examines the impact of variable high-latitude electric fields. Electric fields in the polar ionosphere are primarily due to magnetospheric convection, which results from the interaction between the solar wind and magnetosphere. The convection electric fields in the magnetosphere are transmitted to the polar ionosphere along magnetic field lines. The middle- and low-latitude ionosphere is effectively shielded from the influence of the high-latitude electric field during quiet periods due to the effect of inner magnetospheric shielding [e.g., *Wolf et al.*, 2007]. However, the effectiveness of the shielding depends on magnetospheric conditions, and the incomplete shielding allows the penetration of the polar cap electric field to lower latitudes during active periods [*Nishida*, 1968; *Huang et al.*, 2005; *Kikuchi et al.*, 2008; *Ebihara et al.*, 2014].

Besides, Joule heating associated with the polar-region electrodynamics drives equatorward disturbance winds that produce additional electric fields and currents at middle and low latitudes through the so-called disturbance dynamo mechanism [*Blanc and Richmond*, 1980; *Fuller-Rowell et al.*, 2002]. Electrodynamic effects of the penetration electric field and disturbance dynamo electric field have been extensively studied at equatorial latitudes [*Fejer and Scherliess*, 1995; *Yamazaki and Kosch*, 2015; *Xiong et al.*, 2016] but not well established at other latitudes.

In this study, we examine the relative importance of lower atmospheric forcing and high-latitude forcing in the short-term variability of the dynamo region currents at middle and low latitudes. The investigation is based on numerical simulations by the thermosphere-ionosphere-mesosphere-electrodynamics general circulation model (TIME-GCM) [e.g., *Roble and Ridley*, 1994] for the period 1 – 30 April 2010. Previous numerical studies on the electrodynamic response to lower atmospheric forcing generally assumed constant high-latitude forcing [*Kawano-Sasaki and Miyahara*, 2008; *Jin et al.*, 2011; *Liu et al.*, 2013; *Fang et al.*, 2013; *Yamazaki et al.*, 2014a], and likewise, studies on the electrodynamic response to magnetospheric forcing ignored the effect of variable forcing from the lower atmosphere [e.g., *Maruyama et al.*, 2005; *Klimenko and Klimenko*, 2012; *Marsal et al.*, 2012; *Lu et al.*, 2013]. We take into account short-term variability in both lower atmospheric forcing and high-latitude forcing to address their relative importance. This study also addresses mechanisms by which lower atmospheric forcing and high-latitude forcing modulate the dynamo region currents at middle and low latitudes.

2. Model and Data

2.1. TIME-GCM

The TIME-GCM is a first-principles model of the Earth's upper and middle atmosphere. The model has been developed at the National Center for Atmospheric Research. The reader is referred to *Dickinson et al.* [1984], *Roble et al.* [1988], *Richmond et al.* [1992], and *Roble and Ridley* [1994] and references therein for the

development of the model. Briefly, the TIME-GCM solves the Eulerian continuity, momentum, and energy equations in a spherical coordinate system with latitude and longitude as the horizontal coordinates and constant-pressure surfaces as the vertical coordinate. The pressure interfaces are defined as $Z = \ln(P_0/P)$, where P_0 is a reference pressure height at 5×10^{-7} hPa. The lower and upper boundaries of the model are at $Z = -17$ (12 hPa) and $Z = 7$ (4.6×10^{-10} hPa), respectively. The lower boundary corresponds to approximately 30 km. The height for the upper boundary depends on solar activity, and it is approximately 480 km in the present study for solar minimum conditions. The horizontal resolution of the model is 2.5° × 2.5° in latitude and longitude. The vertical resolution is a quarter scale height, consisting of 97 layers. This is sufficient to accurately resolve large-scale atmospheric waves such as tides and planetary waves.

Electric fields and currents are calculated in the Magnetic Apex coordinates using a realistic geomagnetic field [*Richmond*, 1995b]. The electrodynamics calculations are made in a grid spacing of 4.5° in magnetic longitude and 0.34–3.07° in magnetic latitude, sufficient to resolve the equatorial electrojet. Geomagnetic perturbations at the ground are computed from height-integrated horizontal currents as described by *Richmond and Maute* [2014]. The TIME-GCM takes into account the magnetic effect of secondary currents induced within the Earth. For the calculation of the geomagnetic perturbations due to the induced currents, the model assumes a perfectly conducting layer at 600 km depth where the vertical magnetic perturbations vanish.

The TIME-GCM uses the $F_{10.7}$ index as a solar flux input that determines the heating and ionization rate of the Earth's upper atmosphere [*Solomon and Qian*, 2005]. The solar flux parameterization is largely based on the EUVAC empirical model [*Richards et al.*, 1994], but the soft X-ray fluxes (wavelengths between 8 and 70 Å) are increased by a factor of 4.4 as suggested by *Fang et al.* [2008]. This ad hoc modulation of the soft X-rays achieves a realistically large *E* region plasma density and thus dynamo region currents. *Solomon* [2006] pointed out that the soft X-ray fluxes of the EUVAC model is not as precise as other wavelengths due to the difficulty of accurately measuring in the 8–70 Å range.

For high-latitude forcing, we employ external models that represent the effect of ionosphere-magnetosphere coupling on the high-latitude upper atmosphere. Specifically, the pattern of high-latitude electric fields associated with magnetospheric convection is prescribed by the model of *Heelis et al.* [1982]. Also, energy input associated with particle precipitation in the auroral oval is determined by the model of *Roble and Ridley* [1987]. The hemispheric power and cross polar cap potential to drive these high-latitude models are derived from the *Kp* index using the empirical formula by *Zhang and Paxton* [2008]. The TIME-GCM linearly interpolates 3-hourly *Kp* values to the model time step of 1 min.

Forcing from the lower atmosphere is introduced at the lower boundary of the TIME-GCM (~30 km) by constraining zonal and meridional winds, temperature, and geopotential height with 3-hourly data from the Modern-Era Retrospective Analysis for Research and Application (MERRA) reanalysis [*Rienecker et al.*, 2011]. In this paper, "lower atmospheric forcing" specifically means wave forcing implemented at the lower boundary of the TIME-GCM ~30 km using the MERRA reanalysis. The 3-hourly resolution of the MERRA data enables to resolve short-term variability of diurnal and semidiurnal tidal waves [*Häusler et al.*, 2014]. The lower boundary MERRA forcing mimics the effect that upward propagating tides and planetary waves from the troposphere and stratosphere exert on the upper layers.

2.2. Geomagnetic Data

For the validation of model results, we use ground-based magnetometer data. It should be noted, however, that a direct comparison between observed and simulated magnetic perturbations is difficult during active periods because magnetic perturbations at middle- and low-latitude stations contain signals not only from the dynamo region currents but also from magnetospheric currents, which the TIME-GCM is not able to reproduce. In order to make the model-data comparison possible, we employ the technique developed by *Hibberd* [1981], which substantially eliminates the contribution of magnetospheric currents from the horizontal *H* component of the geomagnetic field. This technique involves a pair of stations that have the same longitude but different latitudes; one station is on the equatorial side of the *Sq* current focus, and the other station is on the polar side of the *Sq* current focus. Since the magnetic perturbations due to distant magnetospheric currents are nearly identical at the two stations, the subtraction of *H* at one station from *H* at the other station leaves only magnetic perturbations due to dynamo region currents. *Xu* [1992] numerically demonstrated that the difference in *H* fields, which we denote as ΔH, is essentially free from the effect of Chapman-Ferraro currents, magnetotail currents, partial and symmetric ring currents, and region 1 and

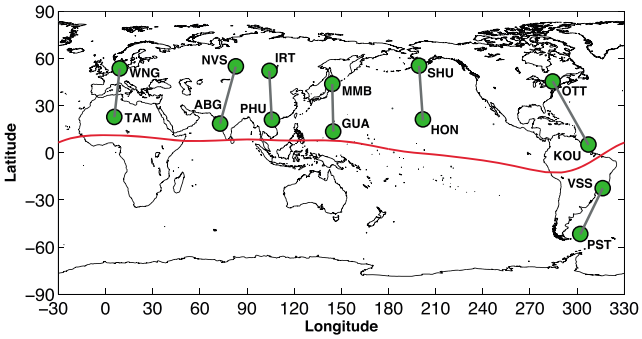

Figure 1. A map of stations used in this study. Names and geographic coordinates of the stations (name, latitude, longitude) are as follows: WNG (Wingst, 53.7°N, 9.1°E), TAM (Tamanrasset, 22.8°N, 5.5°E), NVS (Novosibirsk, 54.9°N, 83.2°E), ABG (Alibag, 18.6°N, 72.9°E), IRT (Irkutsk, 52.2°N, 104.5°E), PHU (Phu Thuy, 21.0°N, 106.0°E), MMB (Memambetsu, 43.9°N, 144.2°E), GUA (Guam, 13.6°N, 144.9°E), SHU (Shumagin, 55.4°N, 199.5°E), HON (Honolulu, 21.3°N, 202.0°E), OTT (Ottawa, 45.4°N, 284.4°E), KOU (Kourou, 5.2°, 307.3°), VSS (Vassouras, −22.4°N, 316.4°E), and PST (Port Stanley, −51.7°N, 302.1°E).

2 field-aligned currents. Hibberd's method has been used by various authors to study *Sq* currents under disturbed conditions [e.g., *Briggs*, 1984; *Takeda and Araki*, 1985; *Hibberd*, 1985; *Stening*, 1995].

We use hourly magnetic data obtained from the World Data Center for Geomagnetism (Edinburgh). Figure 1 shows pairs of stations used in this study. The six pairs of the stations in the Northern Hemisphere well cover various longitude sectors. In the Southern Hemisphere, we found only one pair of stations, because of the small land-to-ocean ratio as well as the lack of suitable lower latitude stations in the African and East Asian sectors.

2.3. Geophysical Conditions and Model Setup

Figure 2 depicts solar and geomagnetic activity during 1–30 April 2010. It can be seen that there is no significant day-to-day variability in solar activity. The $F_{10.7}$ index remained at a low level throughout the month, typical for solar minimum periods. The minimum and maximum values of the $F_{10.7}$ index are 74.5 sfu (solar flux unit; 1 sfu = 10^{-22}W m^{-2} Hz^{-1}) and 79.8 sfu, respectively. Since the range of variations in $F_{10.7}$ is small, our TIME-GCM simulations are run assuming constant solar radiation forcing with the monthly average of the $F_{10.7}$ index (= 76.5 sfu). *Takeda* [1999], comparing *Sq* current systems of the solar minimum year 1964 with those of the solar maximum year 1980, found an increase in the total *Sq* current intensity by approximately 100%. The average $F_{10.7}$ index for 1964 and 1980 is 72.0 sfu and 198.4 sfu, respectively. If this relationship holds for shorter time scales, the change in the total *Sq* current intensity that would be caused by the change in $F_{10.7}$ from 74.5 sfu to 79.8 sfu is estimated to be less than 5%.

Dst and *Kp* indices in Figure 2 reveal quiet to moderately active geomagnetic conditions. There is a geomagnetic storm with the minimum value of the hourly *Dst* index being −81 nT on 6 April. This particular storm was examined using the TIME-GCM by *Lu et al.* [2014] and *Hagan et al.* [2015]. *Lu et al.* [2014] presented model-data comparisons, showing that the model was able to capture the main features of observed thermospheric winds and density during the storm. Their simulation used high-latitude forcing based on the Assimilative Mapping of Ionospheric Electrodynamics (AMIE) [*Richmond and Kamide*, 1988], which specifies high-latitude electrodynamics using various ground and satellite measurements. *Hagan et al.* [2015] examined how tidal signatures in the upper atmosphere could be affected by storm time thermospheric disturbances. In one of the simulations, they used *Kp*-based high-latitude forcing and MERRA lower atmospheric forcing, i.e., the same configuration as the present study. *Hagan et al.* [2015] also conducted a simulation with AMIE high-latitude forcing and MERRA lower atmospheric forcing, showing that tidal response in the thermosphere is qualitatively consistent between the two simulations using *Kp* and AMIE.

We run four simulations. The first simulation uses both *Kp*-based high-latitude forcing and MERRA-based lower atmospheric forcing, which we refer to as Kp_MERRA run. The second simulation uses MERRA forcing, but the high-latitude models (i.e., the electric field model by *Heelis et al.* [1982] and auroral precipitation model by *Roble and Ridley* [1987]) are turned off so that the results will not depend on magnetospheric conditions. We call it noKp_MERRA run. The third simulation uses the *Kp*-driven high-latitude models but in which MERRA forcing is turned off, which we call Kp_noMERRA run. In this case, the seasonally varying background

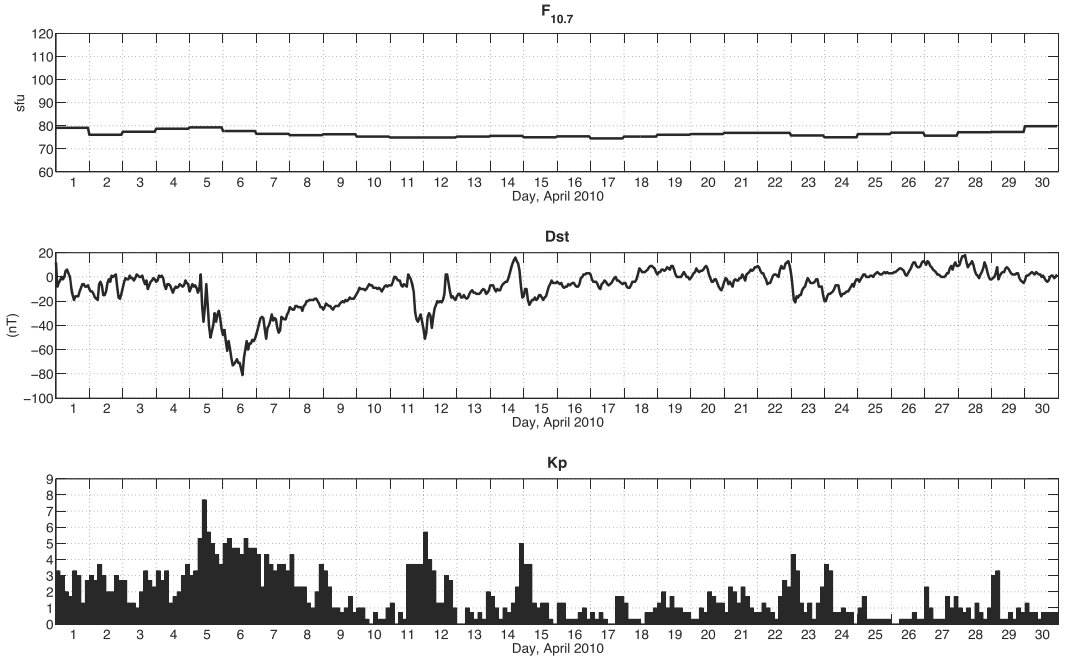

Figure 2. Solar and geomagnetic activity for 1–30 April 2010.

atmosphere is specified at the lower boundary of the model ~30 km. This background atmosphere at the lower boundary does not include any tidal or planetary-wave perturbation; thus, there is no wave forcing from the atmosphere below 30 km. The last simulation uses neither *Kp*-based high-latitude forcing nor MERRA-based lower atmospheric forcing, representing the case where there is no external forcing from the magnetosphere or lower atmosphere. We call it noKp_noMERRA run. The four simulations are summarized in Table 1. As can be seen in the table, the model atmosphere is always subject to solar radiation forcing. Because of that, atmospheric tides arise within the model (30–480 km) even if lower atmospheric forcing is off. Especially, the migrating diurnal tide due to solar ultraviolet heating above 100 km [e.g., *Hagan et al.*, 2001] is effective in producing *Sq* currents.

All the simulations are run from 10 days prior to 1 April 2010 using suitable initial conditions until the end of 30 April 2010. The results from the four simulations are shown in Figure 3, where equivalent current functions averaged over 1–30 April 2010 are plotted as a function of magnetic local time and magnetic latitude. An equivalent current function is a two-dimensional representation of the dynamo region current system. It is the horizontal current system at 110 km that produces the same magnetic perturbations on the ground as the actual three-dimensional current system would. Following *Doumbia et al.* [2007], the equivalent current functions were calculated using global spherical harmonics of order up to $m = 24$ and degree up to $n = 72$. In the figure, equivalent currents of 10 kA flow between adjacent contours. The sign of the equivalent current function was chosen in such a way that the direction of the flow is counterclockwise around a positive

Table 1. Overview of the Simulations Conducted in This Study With the Applied Force in Each Case

Simulation	High-Latitude Forcing[a]	Lower Atmospheric Forcing[b]	Solar Radiation Forcing[c]
Kp_MERRA	Yes	Yes	Yes
Kp_noMERRA	Yes	No	Yes
noKp_MERRA	No	Yes	Yes
noKp_noMERRA	No	No	Yes

[a]By empirical models of the high-latitude electric field [*Heelis et al.*, 1982] and auroral precipitation [*Roble and Ridley*, 1987] driven by the *Kp* index.
[b]By constraining the lower boundary of the model ~30 km with the Modern-Era Retrospective Analysis for Research and Application (MERRA) reanalysis data.
[c]By parameterizations using the daily and 81 day averaged $F_{10.7}$ index.

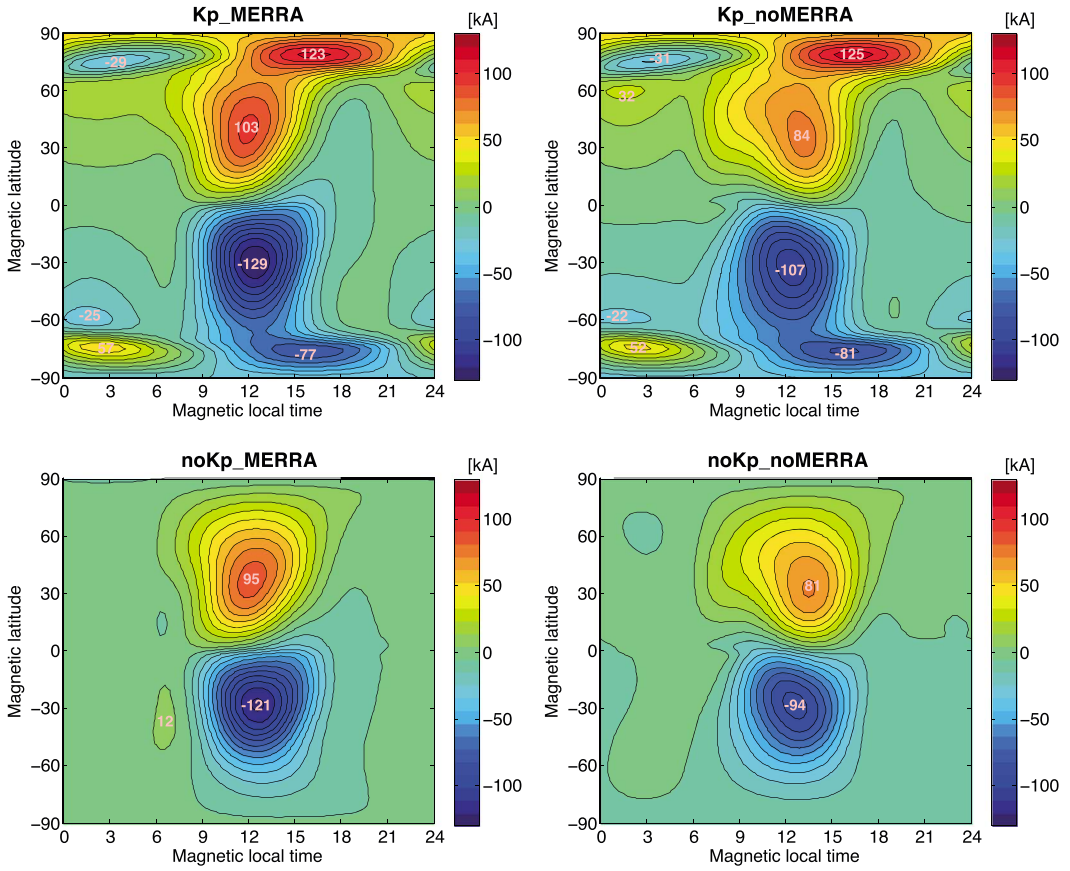

Figure 3. TIME-GCM equivalent current functions averaged over the period 1–30 April 2010 for the (top left) Kp_MERRA run, (top right) Kp_noMERRA run, (bottom left) noKp_MERRA run, and (bottom right) noKp_noMERRA run. An equivalent current of 10 kA flows between contour steps in the counterclockwise direction around positive peaks and in the clockwise direction around negative peaks.

peak and clockwise around a negative peak. The dayside current system, below 60° magnetic latitude, with a counterclockwise vortex in the Northern Hemisphere and clockwise vortex in the Southern Hemisphere, illustrates the well-known *Sq* current system [e.g., *Pedatella et al.*, 2011; *Stening and Winch*, 2013; *Chulliat et al.*, 2016]. The high-latitude current systems above 60° magnetic latitude, known as *DP*2 current systems, represent ionospheric currents driven by high-latitude electric fields. The *DP*2 current systems are visible only in the runs with *Kp*-based high-latitude forcing.

The total *Sq* current intensity, J_{total}, can be defined as the difference between the maximum and minimum values of the equivalent *Sq* current function between ±60° magnetic latitude and between 0600 and 1800 magnetic local time. The quantity represents the total amount of the current that flows between the northern and southern *Sq* foci. J_{total} for the Kp_MERRA run and noKp_noMERRA run are 232 kA and 175 kA, respectively. Therefore, the *Sq* currents produced by magnetospheric and lower atmospheric drivers account for approximately 25% of the total effect. The rest of *Sq* currents is due to solar radiation forcing within the upper and lower boundaries of the model, 30–480 km. According to previous studies, the migrating diurnal tide that is locally generated within the thermosphere (>100 km) explains about a half of the *Sq* current intensity [*Richmond and Roble*, 1987; *Yamazaki et al.*, 2014b].

3. Results and Discussion

3.1. Comparisons With Data

Figure 4 compares observed and simulated Δ*H* for all the pairs of the stations. The simulation results are from the Kp_MERRA run, which include both high-latitude and lower atmospheric forcing. The model-data agreement is generally good. The model well reproduces the pattern and magnitude of the daily variation in Δ*H* in most cases. The correlation coefficient *R* between the observed and simulated Δ*H* is 0.80 or higher, except

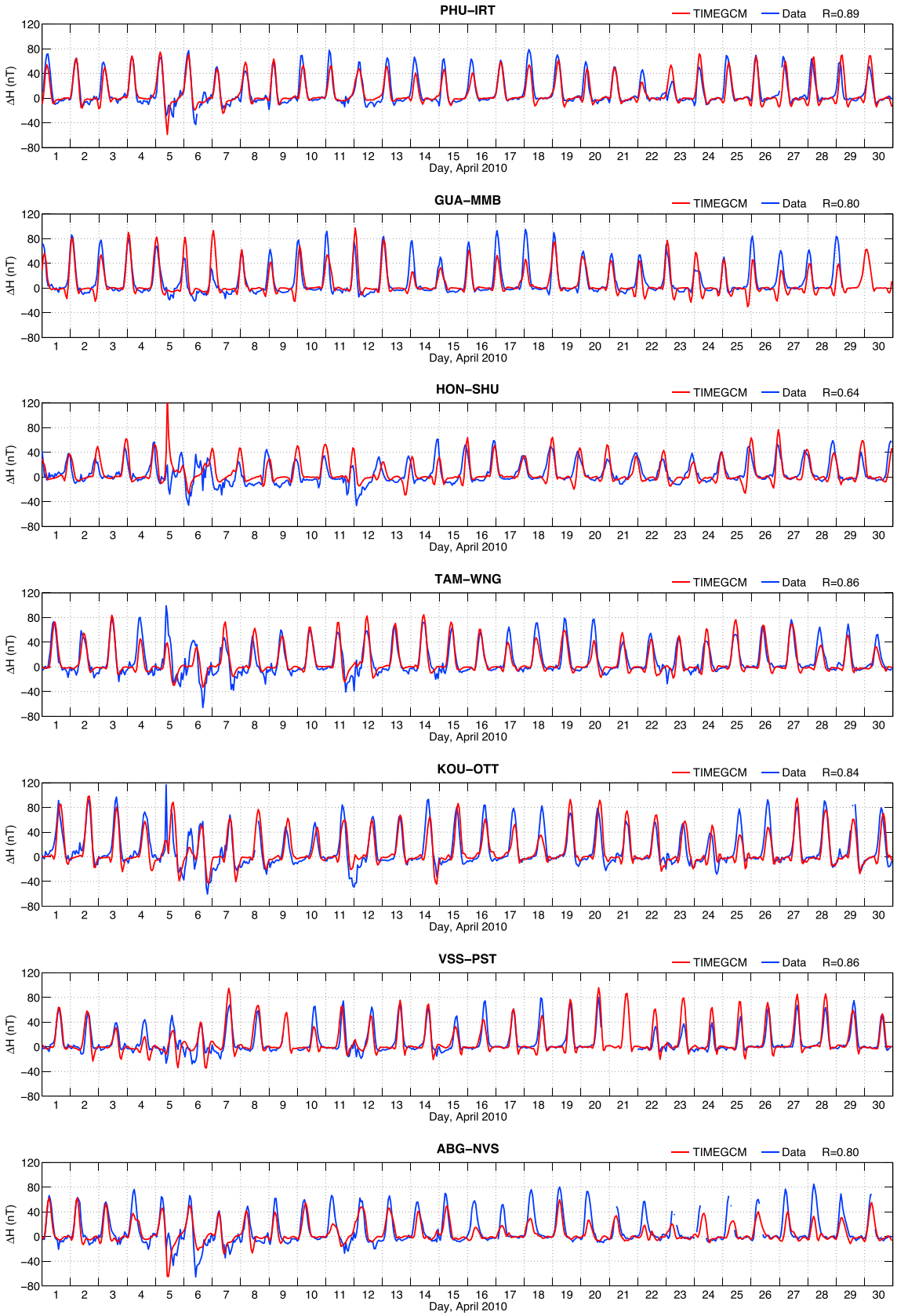

Figure 4. Ground-level magnetic perturbations (blue) observed and (red) simulated by the TIME-GCM for 1–30 April 2010. See Figure 1 for pairs of the stations used.

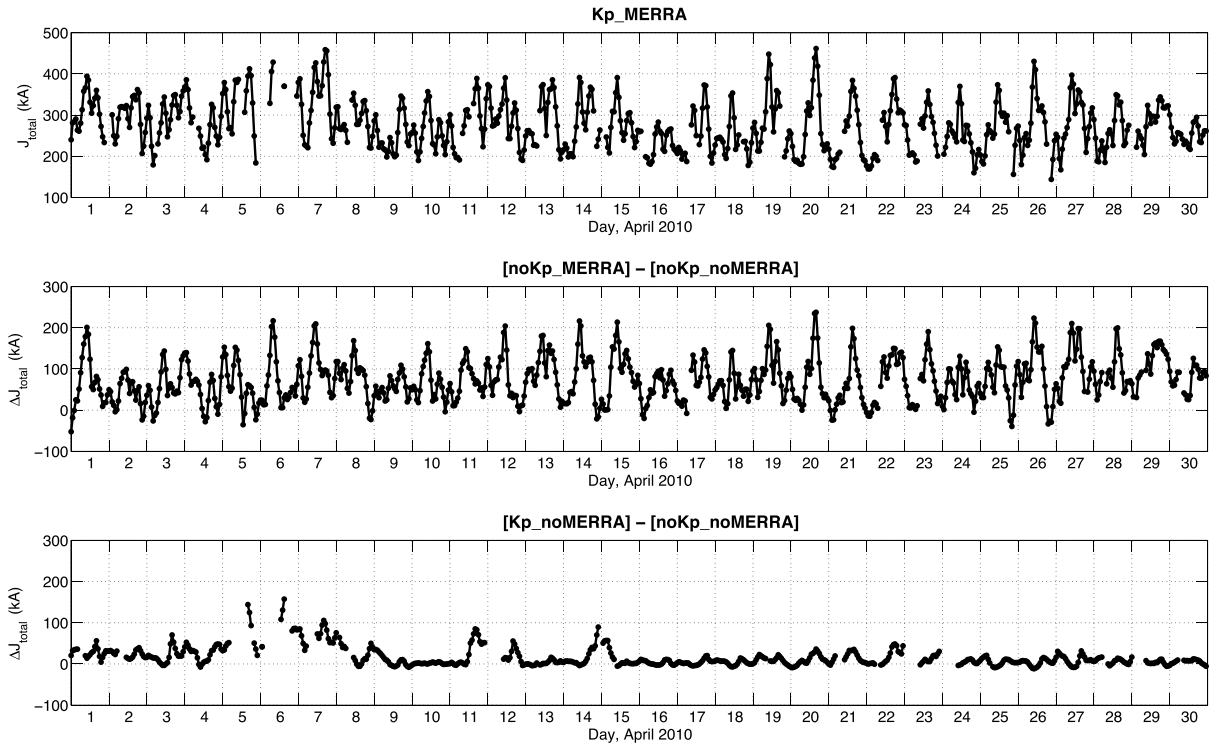

Figure 5. TIME-GCM total *Sq* current intensity J_{total} for 1–30 April 2010. (top) The results for the Kp_MERRA run. (middle) The difference in J_{total} between the noKp_MERRA run and noKp_noMERRA run, representing the effect of lower atmospheric forcing. (bottom) The difference in J_{total} between the Kp_noMERRA run and noKp_noMERRA run, representing the effect of high-latitude forcing.

for the HON-SHU pair where $R = 0.64$. The model partly reproduces disturbance effects during the storm on 5–7 April 2010 as well as day-to-day variations during quiet periods. These results give us confidence that further analysis of the simulation results can provide insight into the mechanism for day-to-day electrodynamic variability.

3.2. Relative Importance of Magnetospheric and Lower Atmospheric Forcing

J_{total} for the Kp_MERRA run is plotted in Figure 5 (top), revealing significant short-term variability in the dynamo region currents. Since we assume constant solar energy input, the day-to-day variation of J_{total} arises primarily from variable magnetospheric and lower atmospheric forcing. The hour-to-hour variation is not only due to temporal changes in the magnetospheric and lower atmospheric drivers but also due to the spatial variation of the main geomagnetic field **B**. At different times of day, different longitudes are on the sunlit side of the Earth where *Sq* currents are produced. The background geomagnetic field affects not only electromotive force $\mathbf{U}\times\mathbf{B}$ (see equation (1)) but also the ionospheric conductivity $\hat{\sigma}$ that tends to change inversely with **B**. These factors lead to the UT variation of the *Sq* current system [e.g., *Stening*, 1971; *Le Sager and Huang*, 2002].

The model-data gaps in Figure 5 are due to the periods when we could not find either or both of the *Sq* foci in the region below 60° magnetic latitude between 0600 and 1800 hours magnetic local time. This occurs, in our simulations, when *DP*2 currents are very strong or when *Sq* currents are very weak. Figure 6 (left) is an example of the equivalent current function where the northern current focus is undetectable owing to strong *DP*2 currents. The results are for the Kp_MERRA run at 0130 UT on 5 April 2010, when $Kp = 4^-$. It can be seen that the westward *Sq* current that flows on the polar side of the northern *Sq* focus is completely canceled out by the eastward current of the dayside *DP*2. In this case, it is not possible to distinguish between the *Sq* and *DP*2 current systems in the Northern Hemisphere; hence, we do not compute J_{total}. The failure in the formation of an *Sq* current vortex also occurs during quiet periods. Figure 6 (right) shows an example, for the case at 1930 UT on 26 April 2010, when $Kp = 0^+$. Earlier studies also found such a disappearance of an *Sq* current vortex during solar minimum years [e.g., *Campbell et al.*, 1993].

One of the experiments we have conducted (but not presented here) revealed that the response of J_{total} to high-latitude and lower atmospheric forcing is essentially linear. That is, high-latitude forcing does not disturb

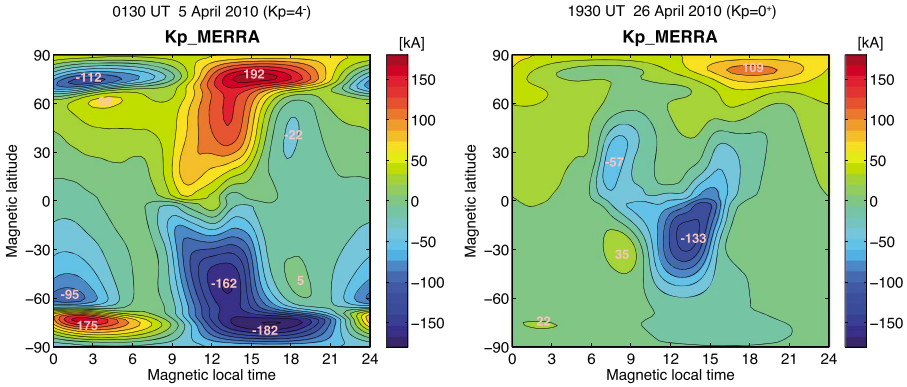

Figure 6. Examples of TIME-GCM equivalent functions when J_{total} is not calculated; (left) the case for 0130 UT on 5 April 2010 and (right) the case for 1930 UT on 26 April 2010.

Sq currents driven by lower atmospheric forcing, nor vice versa. Thus, one can easily separate the effect of high-latitude and lower atmospheric forcing by taking the difference in J_{total} between different simulations (see Table 1). For example, Figure 5 (middle) shows the difference in J_{total} between the noKp_MERRA run and noKp_noMERRA run. In this case, the residuals represent the perturbation in J_{total} due to lower atmospheric forcing. From the comparison with the results in Figure 5 (top), one can see that a large part of short-term variability in J_{total} can be explained as lower atmospheric effects. The correlation coefficient between the two results is 0.78.

Figure 5 (bottom) shows the difference between the Kp_noMERRA run and noKp_noMERRA run, which represents the contribution of magnetospheric drivers. The effect of high-latitude forcing is generally smaller than the effect of lower atmospheric forcing, except during storm periods when the effect of high-latitude forcing tends to be dominant. The comparison with the *Kp* index (Figure 2, bottom) reveals that J_{total} increases with increasing geomagnetic activity. This is probably due to the "leakage" of high-latitude electric fields to lower latitudes.

It is important to note that the TIME-GCM does not have a self-consistent magnetosphere; thus, the model is not able to reproduce the "prompt penetration" electric field associated with rapid changes in the magnetospheric convection. The prompt penetration electric field, however, typically lasts only for ~30 min [*Kikuchi et al.*, 2000; *Peymirat et al.*, 2000]; thus, neglecting the prompt penetration field may not significantly affect the results for hour-to-hour and day-to-day changes in J_{total} presented in Figure 5. In fact, the model reproduces main features of the geomagnetic perturbations during active periods without consideration of the prompt penetration electric field (Figure 4).

The TIME-GCM does take into account the leakage of high-latitude electric fields into lower latitudes due to incomplete steady state shielding. The importance of such a "steady state penetration" electric field has been noted in earlier numerical studies [*Richmond et al.*, 2003; *Zaka et al.*, 2010]. The TIME-GCM also takes into account disturbance winds resulting from Joule heating associated with high-latitude electric fields and currents. It is known that the storm time disturbance winds drive currents that counteract the normal *Sq* current system [*Blanc and Richmond*, 1980; *Le Huy and Amory-Mazaudier*, 2008]. However, the TIME-GCM results during active periods do not show the reduction in J_{total} that is expected from the disturbance dynamo theory. This means that, for the period we investigate, the effect of the steady state penetration electric field dominates over the disturbance dynamo effect at middle and low latitudes where *Sq* currents are produced.

The relative importance of magnetospheric and lower atmospheric forcing for the dynamo region currents depends on geomagnetic activity. Figure 7 presents the difference in J_{total} between the noKp_MERRA run and Kp_noMERRA run as a function of the *Kp* index. If the difference is larger than 0, the amount of the dynamo region currents due to lower atmospheric forcing exceeds the amount of the dynamo region currents due to magnetospheric forcing, and if the difference is less than 0, then the contribution of magnetospheric forcing exceeds the contribution of lower atmospheric forcing. The results in Figure 7 suggest that the contributions of magnetospheric forcing and lower atmospheric forcing are comparable at $Kp = 4^-$. Above this geomagnetic activity level, the high-latitude contribution dominates over the lower atmospheric contribution.

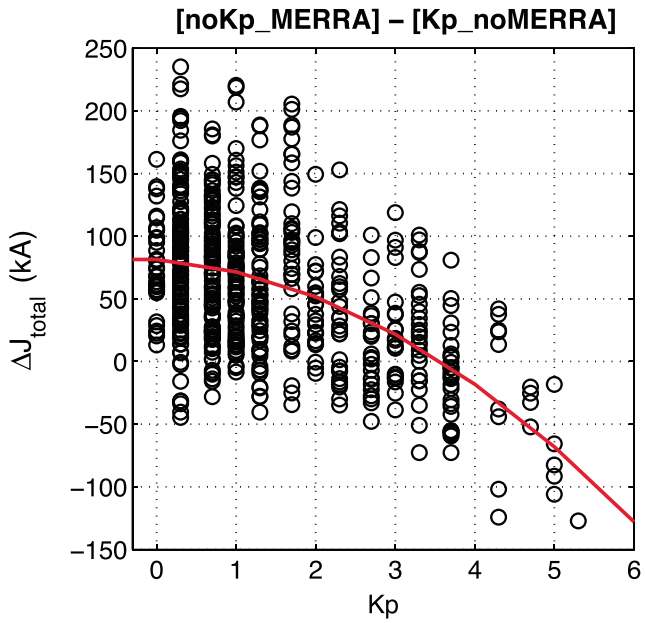

Figure 7. The difference in J_{total} between the noKp_MERRA run and Kp_noMERRA run as a function of the *Kp* index. The best fit curve (second-order polynomial) is also shown in the plot.

3.3. Storm Time Response to Magnetospheric Forcing

In Figure 8, we plot (a, c, and e) equivalent current systems and (b, d, and f) ground-level geomagnetic perturbations in the magnetic northward component for 6 April 2010, when the *Dst* index reached its minimum value. The results are shown as the daily average in the magnetic local time versus magnetic latitude coordinates. Figures 8a and 8b show the results for Kp_MERRA run, while Figures 8c and 8d show the difference between the Kp_noMERRA run and noKp_noMERRA run, depicting only the effect of high-latitude forcing. Figures 8e and 8f show the results for the noKp_MERRA run, illustrating the effect caused by atmospheric tidal forcing. It can be seen in Figure 8c that the penetration electric field drives ionospheric currents not only on the dayside but also on the nightside at middle and low latitudes. This is distinct from the quiet time currents that are confined on the dayside (Figure 8e).

The response of the currents to the penetration electric field is different between the dayside and nightside, which is schematically illustrated in Figure 9. The penetration electric field is mainly eastward on the dayside and westward on the nightside (Figure 9, top row). The penetration electric field rapidly attenuates as it departs from the source polar region on both dayside and nightside (Figure 9, top row). On the dayside, the ionospheric conductivity is highest near the equator, as the plasma density tends to decrease with increasing solar zenith angle. In addition, the effective eastward conductivity is enhanced along the magnetic equator due to the so-called Cowling effect [e.g., *Hirono*, 1950; *Baker and Martyn*, 1953]. The enhanced eastward current gives rise to large-amplitude magnetic perturbations at the magnetic equator as seen in Figure 8d. Observational evidence for the equatorial enhancement of *DP*2 magnetic perturbations can be found in the literature [*Kikuchi et al.*, 1996; *Zaka et al.*, 2009]. Owing to the Cowling effect, the largest response of the currents to the penetration electric field occurs at the magnetic equator (Figure 9, bottom left). Since the ionospheric currents driven by the penetration electric field are not divergence free, charge accumulation occurs to drive additional currents that flow in such a manner as to maintain the current continuity. The resulting current system would have a similar morphology to the normal *Sq* current system with a counterclockwise vortex in the Northern Hemisphere and a clockwise vortex in the Southern Hemisphere (Figure 9, bottom left). Thus, the penetration electric field acts to increase the intensity of the dayside *Sq* current system. The dayside current system in Figure 8c is distorted from the simple *Sq* pattern, especially in the afternoon sector. This could be due to the disturbance dynamo, which acts to drive counter-*Sq* currents on the dayside.

On the nightside, where there is no solar radiation input, the dominant ionization source is the energetic particle precipitation to the auroral oval. At lower latitudes, the ionospheric conductivity is very small at *E* region heights. Therefore, a large response of the currents to the westward penetration electric field is mostly

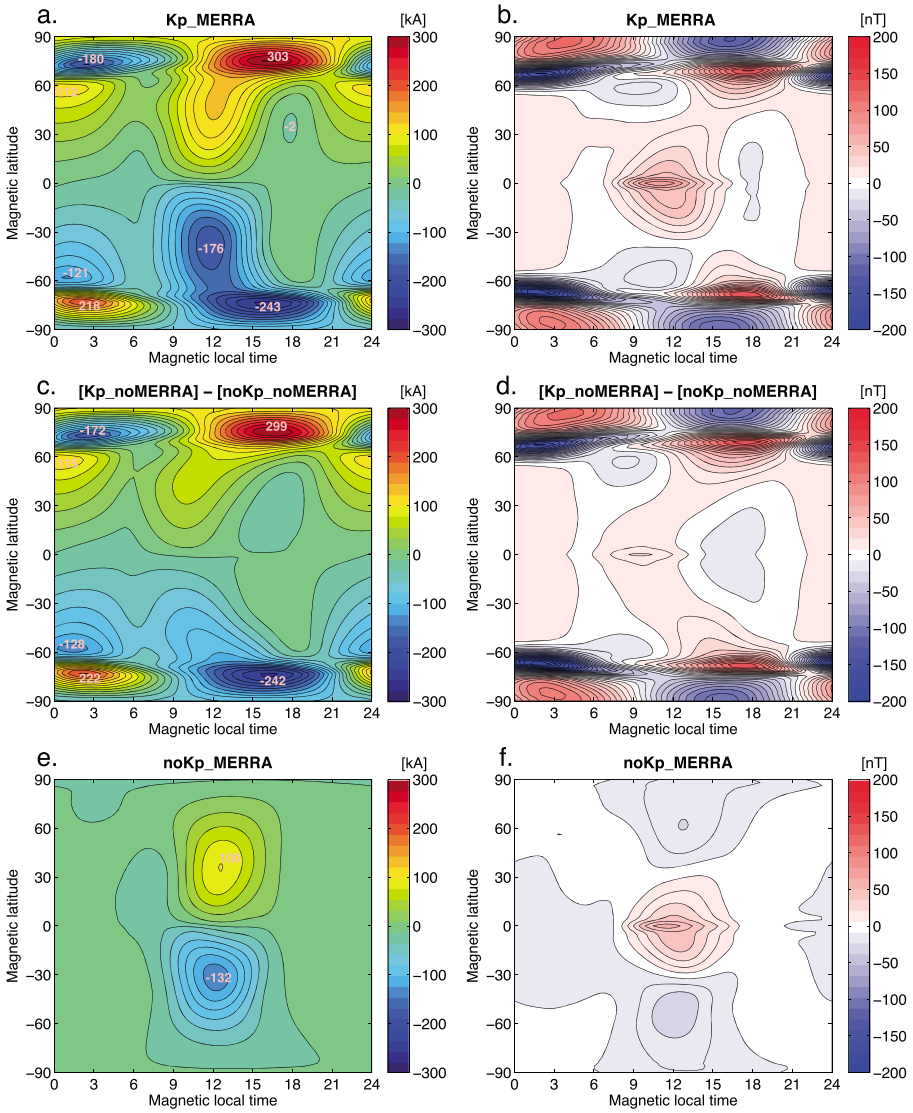

Figure 8. The daily average of the TIME-GCM results for 6 April 2010 as a function of magnetic latitude and magnetic local time. (a, c, e) Equivalent functions and (b, d, f) ground-level magnetic perturbations in the magnetic northward component. Figures 8a and 8b are for the Kp_MERRA run. Figures 8c and 8d are for the difference between Kp_noMERRA run and noKp_noMERRA run, representing the effect of high-latitude forcing. Figures 8e and 8f are for the noKp_MERRA run.

confined to the regions close to the auroral oval (Figure 9, bottom right). The direction of the current is eastward in most parts of middle and low latitudes because the current closure is required for the strong westward currents at high latitudes. The resulting current system resembles the dayside current system, having a counterclockwise vortex in the Northern Hemisphere and a clockwise vortex in the Southern Hemisphere (Figure 9, bottom right). It is interesting to note that the middle- and low-latitude currents caused by the penetration electric field is predominantly eastward on both the dayside and nightside despite the fact that the direction of the penetration electric field is opposite between the dayside and nightside. These eastward dynamo region currents induce northward magnetic perturbations at the surface (Figure 8d). Since the induced magnetic perturbations are northward at most longitudes, they can affect the *Dst* index, which will be evaluated in the following section.

In the discussion above, we considered only the Pedersen currents that flow in the same direction as the electric field. The penetration electric field also drives the Hall currents that flow perpendicular to both the electric field and geomagnetic field, as well as the currents parallel to the geomagnetic field. Thus, the resulting

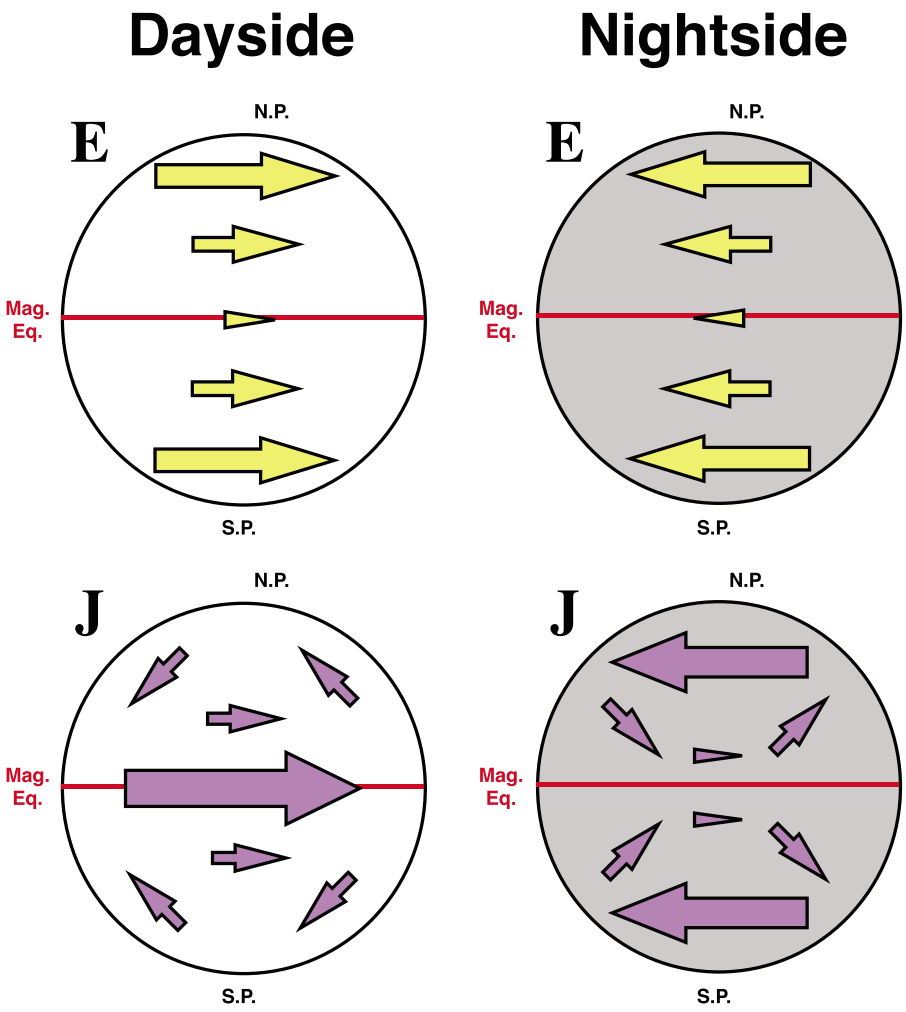

Figure 9. Schematic diagrams describing the storm time response of (top row) electric fields and (bottom row) currents at low and middle latitudes, on the (left column) dayside and (right column) nightside.

current system is three-dimensional. The role of Hall and parallel currents in the normal *Sq* current system was studied by *Fukushima* [1979] and *Takeda* [1991]. More theoretical work is required to understand how the three-dimensional current system arises on the dayside and nightside in response to the penetration electric field.

3.4. Impact on the *Dst* Index

The *Dst* index is widely used as an indicator of geomagnetic storms [*Sugiura*, 1964]. This hourly index represents the zonal mean of the geomagnetic disturbance in the *H* component measured at midlatitude stations. The depression of the *Dst* index during a geomagnetic storm is generally interpreted as a result of the magnetospheric ring current, which flows westward around the Earth and thus reduces the middle- and low-latitude *H* field at all longitudes. This conception, however, has been criticized by *Campbell* [1996, 2004]. He argued that the *Dst* index should not be regarded as a measure of the magnetospheric ring current because the storm time *H* field is affected by other source currents as well. It was suspected that the storm time ionospheric currents might influence the *Dst* index, but no quantitative assessment has been made. Here we discuss the contribution of the storm time ionospheric currents to the *Dst* index based on our TIME-GCM simulation results.

The standard *Dst* index, provided by the World Data Center for Geomagnetism at Kyoto University, uses hourly *H* data from these four stations: Hermanus (HER, 34.4°S, 19.2°E), South Africa; Kakioka (KAK, 36.2°N, 140.2°E), Japan; Honolulu (HON, 21.3°N, 158.0°W), Hawaii; and San Juan (SJG, 18.1°N, 66.2°W), Puerto Rico. At each station, the disturbance time series H_D is calculated by subtracting the background magnetic field and *Sq*

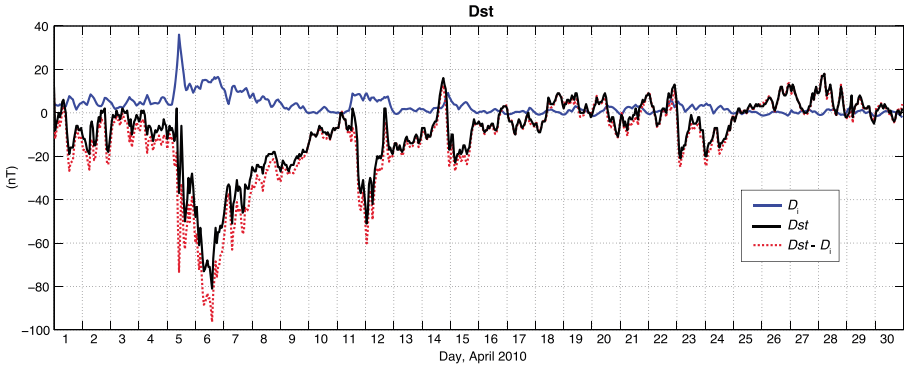

Figure 10. The *Dst* index for 1–30 April. The blue line shows the D_i index derived from the TIME-GCM, representing the ionospheric contribution to the *Dst* index. The black line shows the standard Kyoto *Dst* index. The red line shows the difference between the *Dst* and D_i indicies, representing the magnetospheric contribution to the *Dst* index.

variation from the *H* data. (The day-to-day variation of *Sq* is generally ignored in the data processing.) To derive the *Dst* time series, H_D is averaged over the four stations and normalized to the geomagnetic equator; $Dst = \overline{H_D}/\overline{\cos(\lambda)}$, where λ is geomagnetic latitude and the overbars indicate the arithmetic average over longitude. Although different versions of the *Dst* index exist [e.g., *Karinen and Mursula*, 2005; *Love and Gannon*, 2009], they all follow more or less the same procedures.

For the TIME-GCM results, the disturbance time series H_D can be easily calculated as the difference in *H* between the Kp_noMERRA run and noKp_noMERRA run. Unlike the case for observational data, H_D derived from the model is not subject to the ambiguity due to the determination of *Sq*. We calculate H_D at the locations for HER, KAK, HON, and SJG and derive an hourly index D_i following the same procedures for the *Dst* index. Since the TIME-GCM does not include the magnetosphere, the effect of the ring current is not reproduced by the model. Therefore, D_i reflects purely the effect of ionospheric currents; the subscript *i* represents "ionospheric" currents. In Figure 10, the blue line shows D_i derived from the TIME-GCM, while the black line indicates the standard Kyoto *Dst* index. During quiet periods of the month, D_i is close to zero as there is little ionospheric current associated with high-latitude forcing. During active periods, D_i is elevated because the penetration electric field produces positive perturbations in *H* on both the dayside and nightside as discussed above. The maximum response occurs at the beginning of the storm (D_i =~35 nT). Assuming that the *Dst* index is composed of magnetospheric and ionospheric contributions, the pure magnetospheric component may be derived as $Dst - D_i$, which is shown in Figure 10 by the red dashed line. The results reveal that during storm periods, the *Dst* underestimates the effect of magnetospheric currents, which is represented by $Dst - D_i$. The minimum *Dst* value is −81 nT, while the minimum value of $Dst - D_i$ is −96 nT. Since D_i is primarily due to the penetration of the polar electric field to lower latitudes, D_i is well correlated with the cross polar cap potential (CPCP) in the model. Figure 11 (left) reveals a nonlinear dependence of D_i on CPCP in the TIME-GCM. It may be useful to derive an empirical relationship between the two quantities so that one can estimate D_i from actual measurements of CPCP. The formula for the best fitting second-order polynomial is as follows:

$$D_i = 9.49 \times 10^{-4}(\mathrm{CPCP})^2 + 2.54 \times 10^{-2}(\mathrm{CPCP}) - 0.50 \quad (2)$$

The D_i index can also be estimated using the Polar Cap (*PC*) magnetic activity index [*Troshichev et al.*, 1988], which is known to be dependent on high-latitude electric fields [*Troshichev et al.*, 2000; *Ridley and Kihn*, 2004]. There are *PC* indices for the Northern Hemisphere (*PCN*) and for the Southern Hemisphere (*PCS*), and each of them is derived from magnetic data at a single polar cap station, namely, Thule (77.5°N, 69.2°W), Greenland, for *PCN* and Vostok (78.5°S, 106.9°E), Antarctica, for *PCS*. In Figure 11 (right), we compare D_i with hourly mean values of *PC* index, revealing a good correlation ($R = 0.79$). It is noted that the *PC* index used here is not from the TIME-GCM but from observations. In Figure 11, the average of *PCN* and *PCS* is used because the correlation with D_i is better than when *PCN* or *PCS* is used. The relationship between D_i and *PC* is approximately linear, and the regression line is given as

$$D_i = 2.58 \times PC + 0.52 \quad (3)$$

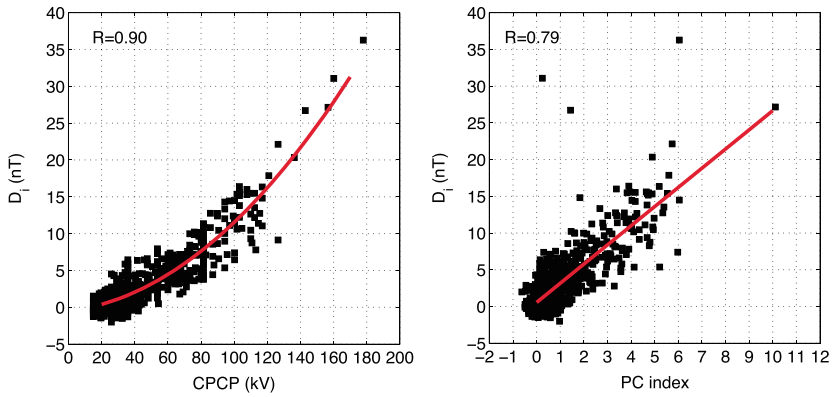

Figure 11. (left) A scatterplot for the D_i index and cross polar cap potential (CPCP) from the TIME-GCM for 1–30 April 2010. (right) A scatterplot for the D_i index and *PC* index ($= \frac{PCN+PCS}{2}$). The *PC* index is based on observations, not the simulation results.

where *PC* is the average of *PCN* and *PCS*. For individual *PCN* and *PCS*, linear regressions are

$$D_i = 2.39 \times PCN + 0.62 \tag{4}$$

$$D_i = 2.57 \times PCS + 0.68 \tag{5}$$

As can be seen in Figure 11 (right), there are a few data points that do not fit well to the regression line. (They are not excluded from fitting.) A close inspection suggests that those outliers appear when the *PC* index shows a rapid change that is not well captured by the model that is driven by 3-hourly *Kp* index.

The empirical formula (2)–(5) could be improved using more accurate high-latitude forcing in the model such as those used by *Marsal et al.* [2012] and *Lu et al.* [2014]. Besides, for the nighttime ionization, the TIME-GCM uses the parameterizations of starlight and geocoronal fluxes that do not depend on location, time of day, season, or solar cycle [*Richmond and Maute*, 2014]. More accurate treatment of nighttime ionization sources will be necessary for a better description of ionospheric currents on the nightside.

It should also be noted that the time period we study in this paper includes only a moderate storm. The response of the middle- and low-latitude ionosphere to high-latitude forcing could be different during a severe storm event, when the inner magnetospheric shielding is often ineffective and the disturbance dynamo effect is more pronounced. A separate study may be necessary for strong storms to evaluate the empirical formula (2)–(5).

3.5. Response to Lower Atmospheric Forcing

As demonstrated in section 3.3, lower atmospheric forcing makes a significant contribution in producing short-term variability of J_{total}. Although previous studies have shown that atmospheric waves from below the dynamo region can modulate middle- and low-latitude *Sq* currents [*Miyahara and Ooishi*, 1997; *Kawano-Sasaki and Miyahara*, 2008], it is not understood which waves play a role and where the currents are generated.

The global wind field in the dynamo region 90–150 km is dominated by atmospheric tides. The tides that have a particularly large amplitude at dynamo region heights are the migrating (i.e., Sun-synchronous) diurnal tide with zonal wave number 1 (DW1), migrating semidiurnal tide with zonal wave number 2 (SW2), and eastward propagating diurnal tide with zonal wave number 3 (DE3) [e.g., *Forbes et al.*, 2008; *Oberheide et al.*, 2011]. We examine the relationship between the day-to-day variation of those tidal waves and the day-to-day variation of J_{total} by analyzing the results for the noKp_MERRA run. The daily amplitude of DW1, SW2, and DE3 is extracted for zonal and meridional winds at various heights. We use a 3 day running window and move it forward in time once a day.

It is conceptually useful to separate the wind field into symmetric and antisymmetric components. For the symmetric component, the eastward wind *u* is symmetric about the geographic equator and the northward

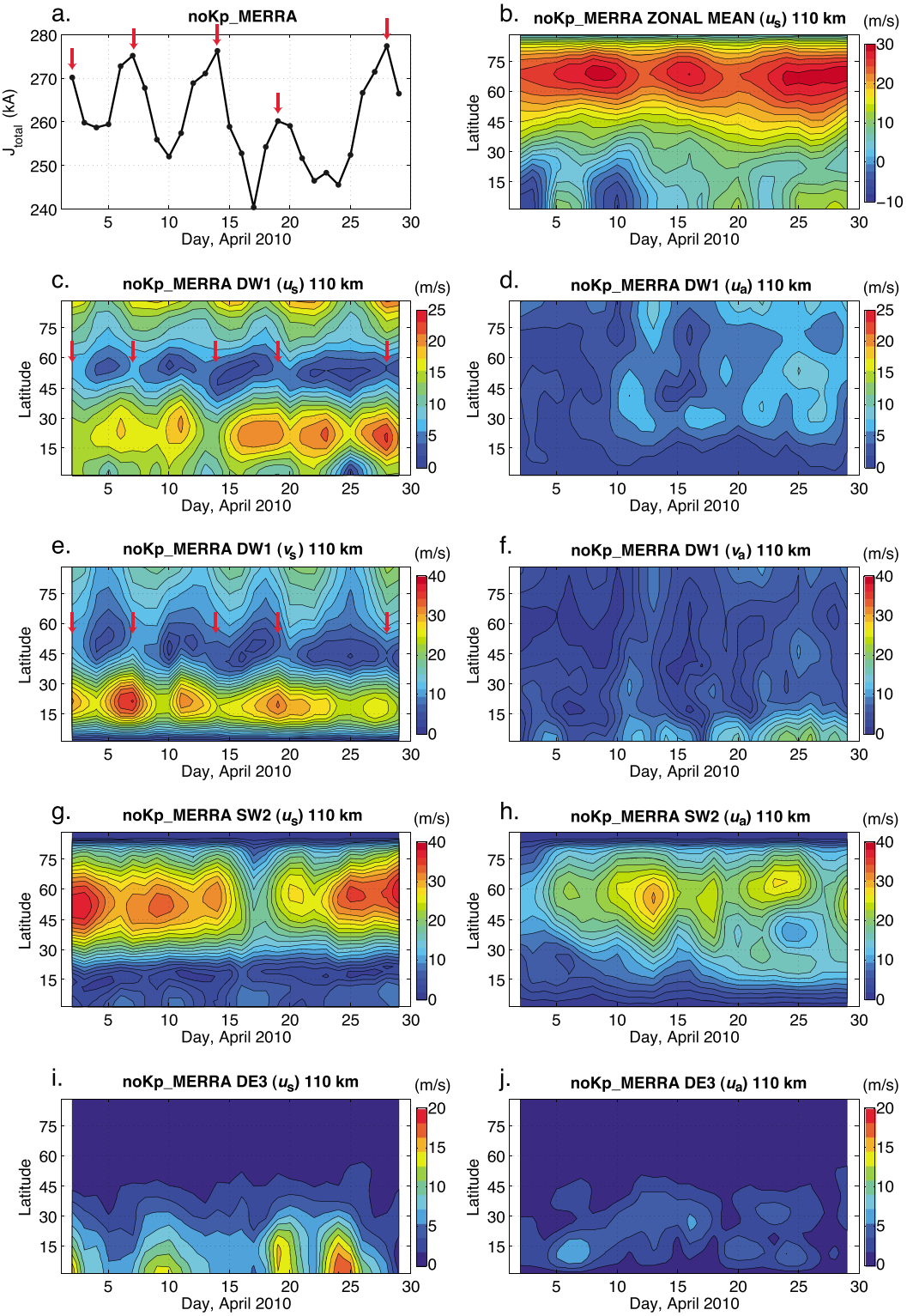

Figure 12. TIME-GCM ionospheric currents and neutral winds at 110 km. The results are for (a) J_{total}; (b) zonal mean zonal wind in u_s; the amplitude of (c) migrating diurnal tide (DW1) in u_s, (d) DW1 in u_a, (e) DW1 in v_s, and (f) DW1 in v_a; the amplitude of (g) migrating semidiurnal tide (SW2) in u_s and (h) SW2 in u_a; and the amplitude of (i) eastward propagating diurnal tide with wave number 3 (DE3) in u_s and (j) DE3 in u_a. u and v denote eastward and northward winds, respectively. The subscripts s and a represent symmetric and antisymmetric components, respectively (see equations (6) and (7)).

wind v changes the sign at the equator. On the other hand, for the antisymmetric component, v is symmetric about the equator and u changes the sign at the equator. The wind field is thus

$$\mathbf{U}_s = \begin{pmatrix} u_s(\phi) \\ v_s(\phi) \end{pmatrix} = \begin{pmatrix} \frac{u(\phi)+u(-\phi)}{2} \\ \frac{v(\phi)-v(-\phi)}{2} \end{pmatrix} \tag{6}$$

$$\mathbf{U}_a = \begin{pmatrix} u_a(\phi) \\ v_a(\phi) \end{pmatrix} = \begin{pmatrix} \frac{u(\phi)-u(-\phi)}{2} \\ \frac{v(\phi)+v(-\phi)}{2} \end{pmatrix} \tag{7}$$

where ϕ denotes latitude in degree. The subscripts s and a represent symmetric and antisymmetric components, respectively. The symmetric and antisymmetric winds tend to produce symmetric and antisymmetric current systems, respectively [*Stening*, 1989; *Yamazaki et al.*, 2012]. The symmetric winds are more effective in changing J_{total}. The antisymmetric winds tend to modulate the *Sq* current system in such a manner as they strengthen the current intensity in one hemisphere and weaken it in the other hemisphere, which does not change J_{total}. Moreover, the ionospheric currents driven by the antisymmetric winds tend to close the current system by connecting with interhemispheric field-aligned currents [*Park et al.*, 2011; *Lühr et al.*, 2015] that do not change J_{total}. Although geographically symmetric and antisymmetric winds are not entirely symmetric or antisymmetric in magnetic coordinates, the symmetric and antisymmetric properties of the winds tend to dominate even after coordinate conversion.

Figure 12a illustrates the 3 day average of J_{total} for the noKp_MERRA run, revealing rises and falls in J_{total}. The local peaks are indicated by the arrows. Figure 12b displays the zonal mean zonal wind of the symmetric eastward wind. The results show short-term variability in the mean flow, especially in the latitude ranges 0–15° and 60–75°. However, neither of these variations correlates with the day-to-day change in J_{total}. Earlier studies also found that the zonal mean flow makes little contribution to *Sq* currents [*Kato*, 1957; *Richmond et al.*, 1976].

The short-term variability in the migrating diurnal tide DW1 is presented in Figure 12c for the symmetric eastward wind, in Figure 12d for the antisymmetric eastward wind, in Figure 12e for the symmetric northward wind, and in Figure 12f for the antisymmetric northward wind. It is noted that different color scales are used for the results of eastward and northward winds. The amplitude of DW1 is generally greater in symmetric winds than antisymmetric winds. Both symmetric and antisymmetric winds show short-term variability. The symmetric component shows the day-to-day variation that resembles the day-to-day variation of J_{total}. The red arrows in Figures 12c and 12e indicate the time when J_{total} shows local peaks. The maximum correlation between J_{total} and the amplitude of the symmetric DW1 winds occurs at 56° latitude ($R = 0.52$) for the eastward wind and at 46° latitude ($R = 0.54$) for the northward wind. Also, the height where the correlation peaks is at 111 km for the eastward wind and at 118 km for the northward wind.

Figures 12g and 12h show the amplitude of the migrating semidiurnal tide SW2 in the eastward symmetric and antisymmetric winds, respectively. There is a prominent reduction in the symmetric SW2 amplitude at 45–60° latitude on 17 April 2010, which corresponds well with the reduction of J_{total} on the same day. The reason for the SW2 reduction is unclear. Peaks in the antisymmetric component do not match those in J_{total}. Figures 12i and 12j show the same but for the eastward propagating diurnal tide with zonal wave number 3 (DE3). The amplitude of the DE3 winds peaks near the equator, which is known to have a significant impact on the equatorial electric field and current [e.g., *Jin et al.*, 2008; *Fang et al.*, 2013]. However, neither symmetric nor antisymmetric component correlates with J_{total}.

The above results suggest that the day-to-day variation in J_{total} is dominated by symmetric-mode migrating diurnal and semidiurnal tidal winds at 45–60° latitude at ~110 km. It is out of the scope of this study to identify the mechanism for the day-to-day variation of the dynamo region tides. According to previous studies, short-term tidal variability can occur due to the presence of planetary waves [e.g., *Liu et al.*, 2010; *Chang et al.*, 2011; *Maute et al.*, 2014], due to changes in the mean flow [e.g., *Stening et al.*, 1997; *Pedatella et al.*, 2012], and due to changes in the tidal sources [e.g., *Goncharenko et al.*, 2012]. In our simulation results, the DW1 amplitude has four to five peaks within a month, and thus, planetary waves with periods of 6–7.5 days [e.g., *Lieberman et al.*, 2003; *Liu et al.*, 2004] may be involved. Since atmospheric tides and planetary waves are highly seasonally dependent, different waves could play a role for short-term *Sq* variability at different seasons. The effect of

solar activity also remains to be investigated. Other studies showed that equatorial electrodynamic response to lower atmospheric forcing depends on solar activity [e.g., *Liu and Richmond*, 2013; *Fang et al.*, 2014].

4. Conclusions

TIME-GCM simulations have been performed for 1–30 April 2010. The model was run with a constant solar energy input but with variable forcing at high latitudes and at the lower boundary (~30 km). The model well reproduced ground-level magnetic perturbations at middle and low latitudes. The main results of this study are as follows:

1. Lower atmospheric forcing is responsible for the major part of short-term variability in the total *Sq* current intensity. The contribution of high-latitude forcing is generally small except during active periods ($Kp \geq 4$).
2. The total *Sq* current intensity increases with increasing geomagnetic activity as high-latitude electric fields leak to lower latitudes. During storm periods, the penetration electric field drives ionospheric currents not only on the dayside but also on the nightside, which affects the *Dst* index.
3. The effect of ionospheric currents to the *Dst* index is evaluated, and empirical formula (equations (2)–(5)) are presented to estimate this effect using the *PC* index and the cross polar cap potential. More simulation work is required to verify these empirical formula for different storms.
4. The quiet time day-to-day variation of the total *Sq* current intensity is dominated by symmetric-mode diurnal and semidiurnal migrating tides in neutral winds at 45–60° latitude at ~110 km. More studies are necessary to understand seasonal and solar activity effects on the short-term *Sq* variability.

Acknowledgments
We thank A. Maute for reviewing a draft manuscript and for useful comments. The geomagnetic field data were provided by the World Data Center for Geomagnetism, Edinburgh. The solar activity index $F_{10.7}$ was provided by the Herzberg Institute of Astrophysics. The geomagnetic indices *Kp* and *Dst* were provided by the World Data Center for Geomagnetism, Kyoto. The *PC* magnetic index was provided by http://pc-index.org. The numerical data from the simulations will be made available upon request. K.H. was supported by the Advanced Study Program Postdoctoral Fellowship of the National Center for Atmospheric Research. The National Center for Atmospheric Research is sponsored by the National Science Foundation. J.A.W. was supported by Natural Environment Research Council grant NE/J021792/1.

References

Baker, W. G., and D. F. Martyn (1953), Electric currents in the ionosphere. I. The conductivity, *Philos. Trans. R. Soc. London, Ser. A*, *246*, 281–294.
Blanc, M., and A. D. Richmond (1980), The ionospheric disturbance dynamo, *J. Geophys. Res.*, *85*(A4), 1669–1686, doi:10.1029/JA085iA04p01669.
Briggs, B. H. (1984), The variability of ionospheric dynamo currents, *J. Atmos. Terr. Phys.*, *46*, 419–429.
Campbell, W. H. (1989), An introduction to quiet daily geomagnetic fields, *Pure Appl. Geophys.*, *131*(3), 315–331.
Campbell, W. H. (1996), Geomagnetic storms, the *Dst* ring-current myth and lognormal distributions, *J. Atmos. Sol. Terr.*, *58*, 1171–1187.
Campbell, W. H. (2004), Failure of *Dst* index fields to represent a ring current, *Space Weather*, *2*, S08002, doi:doi:10.1029/2003SW000041.
Campbell, W. H., and S. Matsushita (1982), *Sq* currents: A comparison of quiet and active year behavior, *J. Geophys. Res.*, *87*(A7), 5305–5308.
Campbell, W. H., B. R. Arora, and E. R. Schiffmacher (1993), External *Sq* currents in the India? Siberia region, *J. Geophys. Res.*, *98*, 3741–3752.
Chang, L. C., S. E. Palo, and H.-L. Liu (2011), Short-term variability in the migrating diurnal tide caused by interactions with the quasi 2 day wave, *J. Geophys. Res.*, *116*, D12112, doi:10.1029/2010JD014996.
Chulliat, A., P. Vigneron, E. Thébault, O. Sirol, and G. Hulot (2013), Swarm SCARF dedicated ionospheric field inversion chain, *Earth Planets Space*, *65*, 1271–1283.
Chulliat, A., P. Vigneron, and G. Hulot (2016), First results from the Swarm dedicated ionospheric field inversion chain, *Earth Planets Space*, *68*, 1–18, doi:10.1186/s40623-016-0481-6.
Dickinson, R. E., E. C. Ridley, and R. G. Roble (1984), Thermospheric general circulation with coupled dynamics and composition, *J. Atmos. Sci.*, *41*, 205–219.
Doumbia, V., A. Maute, and A. D. Richmond (2007), Simulation of equatorial electrojet magnetic effects with the thermosphere-ionosphere-electrodynamics general circulation model, *J. Geophys. Res.*, *112*, A09309, doi:10.1029/2007JA012308.
Ebihara, Y., T. Tanaka, and T. Kikuchi (2014), Counter equatorial electrojet and overshielding after substorm onset: Global MHD simulation study, *J. Geophys. Res. Space Physics*, *119*, 7281–7296, doi:10.1002/2014JA020065.
Fang, T.-W., A. D. Richmond, J. Y. Liu, A. Maute, C. H. Lin, C. H. Chen, and B. Harper (2008), Model simulation of the equatorial electrojet in the Peruvian and Philippine sectors, *J. Atmos. Sol. Terr. Phys.*, *70*, 2203–2211, doi:10.1016/j.jastp.2008.04.021.
Fang, T.-W., R. Akmaev, T. Fuller-Rowell, F. Wu, N. Maruyama, and G. Millward (2013), Longitudinal and day-to-day variability in the ionosphere from lower atmosphere tidal forcing, *Geophys. Res. Lett.*, *40*, 2523–2528, doi:10.1002/grl.50550.
Fang, T.-W., T. Fuller-Rowell, H. Wang, R. Akmaev, and F. Wu (2014), Ionospheric response to sudden stratospheric warming events at low and high solar activity, *J. Geophys. Res. Space Physics*, *119*, 7858–7869, doi:10.1002/ 2014JA020142.
Fejer, B. G., and L. Scherliess (1995), Time-dependent response of equatorial ionospheric electric fields to magnetospheric disturbances, *Geophys. Res. Lett.*, *22*, 851–854, doi:10.1029/95GL00390.
Forbes, J. M., X. Zhang, S. Palo, J. Russell, C. J. Mertens, and M. Mlynczak (2008), Tidal variability in the ionospheric dynamo region, *J. Geophys. Res.*, *113*, A02310, doi:10.1029/2007JA012737.
Fukushima, N. (1979), Electric potential difference between conjugate points in middle latitudes caused by asymmetric dynamo in the ionosphere, *J. Geomagn. Geoelectr.*, *31*, 401–409.
Fuller-Rowell, T. J., G. H. Millward, A. D. Richmond, and M. V. Codrescu (2002), Storm-time changes in the upper atmosphere at low latitudes, *J. Atmos. Sol. Terr. Phys.*, *64*, 1383–1391.
Goncharenko, L. P., A. J. Coster, R. A. Plumb, and D. I. V. Domeisen (2012), The potential role of stratospheric ozone in the stratosphere-ionosphere coupling during stratospheric warmings, *Geophys. Res. Lett.*, *39*, L08101, doi:10.1029/ 2012GL051261.
Hagan, M. E., R. G. Roble, and J. Hackney (2001), Migrating thermospheric tides, *J. Geophys. Res.*, *106*, 12,739–12,752.
Hagan, M. E., K. Häusler, G. Lu, J. M. Forbes, and X. Zhang (2015), Upper thermospheric responses to forcing from above and below during 1–10 April 2010: Results from an ensemble of numerical simulations, *J. Geophys. Res. Space Physics*, *120*, 3160–3174, doi:10.1002/2014JA020706.
Hasegawa, M. (1960), On the position of the focus of the geomagnetic *Sq* current system, *J. Geophys. Res.*, *65*(5), 1437–1447, doi:10.1029/JZ065i005p01437.

Häusler, K., M. E. Hagan, A. J. G. Baumgaertner, A. Maute, G. Lu, E. Doornbos, S. Bruinsma, J. M. Forbes, and F. Gasperini (2014), Improved short-term variability in the thermosphere-ionosphere-mesosphere-electrodynamics general circulation model, *J. Geophys. Res. Space Physics*, *119*, 6623–6630, doi:10.1002/2014JA020006.

Heelis, R. A., J. K. Lowell, and R. W. Spiro (1982), A model of the high-latitude ionospheric convection pattern, *J. Geophys. Res.*, *87*, 6339–6345.

Hibberd, F. H. (1981), Day-to-day variability of the *Sq* geomagnetic field variation, *Aust. J. Phys.*, *34*, 81–90.

Hibberd, F. H. (1985), The geomagnetic *Sq* variation—Annual, semi-annual and solar cycle variations and ring current effects, *J. Atmos. Terr. Phys.*, *47*, 341–352.

Hirono, M. (1950), On the influence of the Hall current to the electrical conductivity of the ionosphere. I, *J. Geomagn. Geoelectr.*, *2*, 1–8.

Huang, C.-S., J. C. Foster, and M. C. Kelley (2005), Long-duration penetration of the interplanetary electric field to the low-latitude ionosphere during the main phase of magnetic storms, *J. Geophys. Res.*, *110*, A11309, doi:10.1029/2005JA011202.

Jin, H., Y. Miyoshi, H. Fujiwara, and H. Shinagawa (2008), Electrodynamics of the formation of ionospheric wave number 4 longitudinal structure, *J. Geophys. Res.*, *113*, A09307, doi:10.1029/2008JA013301.

Jin, H., Y. Miyoshi, H. Fujiwara, H. Shinagawa, K. Terada, N. Terada, M. Ishii, Y. Otsuka, and A. Saito (2011), Vertical connection from the tropospheric activities to the ionospheric longitudinal structure simulated by a new Earth's whole atmosphere-ionosphere coupled model, *J. Geophys. Res.*, *116*, A01316, doi:10.1029/2010JA015925.

Karinen, A., and K. Mursula (2005), A new reconstruction of the *Dst* index for 1932–2002, *Ann. Geophys.*, *23*, 475–485.

Kato, S. (1957), Prevailing wind in the ionosphere and geomagnetic *Sq* variations, *J. Geomagn. Geoelectr.*, *9*, 215–217.

Kawano-Sasaki, K., and S. Miyahara (2008), A study on three-dimensional structures of the ionospheric dynamo currents induced by the neutral winds simulated by the Kyushu-GCM, *J. Atmos. Sol. Terr. Phys.*, *70*, 1549–1562.

Kikuchi, T., H. Lühr, T. Kitamura, O. Saka, and K. Schlegel (1996), Direct penetration of the polar electric field to the equator during a *DP* 2 event as detected by the auroral and equatorial magnetometer chains and the EISCAT radar, *J. Geophys. Res.*, *101*(A8), 17,161–17,173, doi:10.1029/96JA01299.

Kikuchi, T., H. Lühr, K. Schlegel, H. Tachihara, M. Shinohara, and T.-I. Kitamura (2000), Penetration of auroral electric fields to the equator during a substorm, *J. Geophys. Res.*, *105*(A10), 23,251–23,261, doi:10.1029/2000JA900016.

Kikuchi, T., K. K. Hashimoto, and K. Nozaki (2008), Penetration of magnetospheric electric fields to the equator during a geomagnetic storm, *J. Geophys. Res.*, *113*, A06214, doi:10.1029/2007JA012628.

Klimenko, M. V., and V. V. Klimenko (2012), Disturbance dynamo, prompt penetration electric field and overshielding in the Earth's ionosphere during geomagnetic storm, *J. Atmos. Sol. Terr. Phys.*, *90–91*, 146–155.

Le Huy, M., and C. Amory-Mazaudier (2008), Planetary magnetic signature of the storm wind disturbance dynamo currents: D_{dyn}, *J. Geophys. Res.*, *113*, A02312, doi:10.1029/2007JA012686.

Le Sager, P., and T. S. Huang (2002), Longitudinal dependence of the daily geomagnetic variation during quiet time, *J. Geophys. Res.*, *107*(A11), 1397, doi:10.1029/2002JA009287.

Lieberman, R. S., D. M. Riggin, S. J. Franke, A. H. Manson, C. Meek, T. Nakamura, T. Tsuda, R. A. Vincent, and I. Reid (2003), The 6.5-day wave in the mesosphere and lower thermosphere: Evidence for baroclinic/barotropic instability, *J. Geophys. Res.*, *108*(D20), 4640, doi:10.1029/2002JD003349.

Liu, H.-L. (2014), WACCM-X simulation of tidal and planetary wave variability in the upper atmosphere, in *Modeling the Ionosphere-Thermosphere System*, edited by J. Huba, R. Schunk, and G. Khazanov, John Wiley, Chichester, U. K., doi:10.1002/9781118704417.ch16

Liu, H.-L., and A. D. Richmond (2013), Attribution of ionospheric vertical plasma drift perturbations to large-scale waves and the dependence on solar activity, *J. Geophys. Res. Space Physics*, *118*, 2452–2465, doi:10.1002/jgra.50265.

Liu, H.-L., E. R. Talaat, R. G. Roble, R. S. Lieberman, D. M. Riggin, and J.-H. Yee (2004), The 6.5-day wave and its seasonal variability in the middle and upper atmosphere, *J. Geophys. Res.*, *109*, D21112, doi:10.1029/2004JD004795.

Liu, H.-L., W. Wang, A. D. Richmond, and R. G. Roble (2010), Ionospheric variability due to planetary waves and tides for solar minimum conditions, *J. Geophys. Res.*, *115*, A00G01, doi:10.1029/2009JA015188.

Liu, H.-L., V. A. Yudin, and R. G. Roble (2013), Day-to-day ionospheric variability due to lower atmosphere perturbations, *Geophys. Res. Lett.*, *40*, 665–670, doi:10.1002/grl.50125.

Love, J. J., and J. L. Gannon (2009), Revised *Dst* and the epicycles of magnetic disturbance: 1958–2007, *Ann. Geophys.*, *27*, 3101–3131.

Lu, G., J. D. Huba, and C. Valladares (2013), Modeling ionospheric super-fountain effect based on the coupled TIMEGCM-SAMI3, *J. Geophys. Res. Space Physics*, *118*, 2527–2535, doi:10.1002/jgra.50256.

Lu, G., M. E. Hagan, K. Häusler, E. Doornbos, S. Bruinsma, B. J. Anderson, and H. Korth (2014), Global ionospheric and thermospheric response to the 5 April 2010 geomagnetic storm: An integrated data-model investigation, *J. Geophys. Res. Space Physics*, *119*, 10,358–10,375, doi:10.1002/2014JA020555.

Lühr, H., G. Kervalishvili, I. Michaelis, J. Rauberg, P. Ritter, J. Park, J. M. G. Merayo, and P. Brauer (2015), The interhemispheric and *F* region dynamo currents revisited with the Swarm constellation, *Geophys. Res. Lett.*, *42*, 3069–3075, doi:10.1002/2015GL063662.

Marsal, S., A. D. Richmond, A. Maute, and B. J. Anderson (2012), Forcing the TIEGCM model with Birkeland currents from the Active Magnetosphere and Planetary Electrodynamics Response Experiment, *J. Geophys. Res.*, *117*, A06308, doi:10.1029/2011JA017416.

Maruyama, N., A. D. Richmond, T. J. Fuller-Rowell, M. V. Codrescu, S. Sazykin, F. R. Toffoletto, R. W. Spiro, and G. H. Millward (2005), Interaction between direct penetration and disturbance dynamo electric fields in the storm-time equatorial ionosphere, *Geophys. Res. Lett.*, *32*, L17105, doi:10.1029/2005GL023763.

Maute, A., M. E. Hagan, A. D. Richmond, and R. G. Roble (2014), TIME-GCM study of the ionospheric equatorial vertical drift changes during the 2006 stratospheric sudden warming, *J. Geophys. Res. Space Physics*, *119*, 1287–1305, doi:10.1002/2013JA019490.

Miyahara, S., and M. Ooishi (1997), Variation of *Sq* induced by atmospheric tides simulated by a middle atmosphere general circulation model, *J. Geomagn. Geoelectr.*, *49*, 77–87.

Nishida, A. (1968), Coherence of DP2 fluctuations with interplanetary magnetic field variations, *J. Geophys. Res.*, *73*, 5549–5559.

Oberheide, J., J. M. Forbes, X. Zhang, and S. L. Bruinsma (2011), Climatology of upward propagating diurnal and semidiurnal tides in the thermosphere, *J. Geophys. Res.*, *116*, A11306, doi:10.1029/2011JA016784.

Park, J., H. Lühr, and K. W. Min (2011), Climatology of the inter-hemispheric field-aligned current system in the equatorial ionosphere as observed by CHAMP, *Ann. Geophys.*, *29*, 573–582, doi:10.5194/angeo-29-573-2011.

Pedatella, N. M., J. M. Forbes, and A. D. Richmond (2011), Seasonal and longitudinal variations of the solar quiet (*Sq*) current system during solar minimum determined by CHAMP satellite magnetic field observations, *J. Geophys. Res.*, *116*, A04317, doi:10.1029/2010JA016289.

Pedatella, N. M., H.-L. Liu, A. D. Richmond, A. Maute, and T.-W. Fang (2012), Simulations of solar and lunar tidal variability in the mesosphere and lower thermosphere during sudden stratosphere warmings and their influence on the low-latitude ionosphere, *J. Geophys. Res.*, *117*, A08326, doi:10.1029/2012JA017858.

Peymirat, C., A. D. Richmond, and A. T. Kobea (2000), Electrodynamic coupling of high and low latitudes: Simulations of shielding/overshielding effects, *J. Geophys. Res.*, *105*(A10), 22991–23003, doi:10.1029/2000JA000057.

Richards, P. G., J. A. Fennelly, and D. G. Torr (1994), EUVAC: A solar EUV flux model for aeronomic calculations, *J. Geophys. Res.*, *99*(A5), 8981–8992, doi:10.1029/94JA00518.

Rienecker, M. M., et al. (2011), MERRA: NASAś modern-era retrospective analysis for research and applications, *J. Clim.*, *24*, 3624–3648, doi:10.1175/JCLI-D-11-00015.1.

Richmond, A. D. (1995a), Ionospheric electrodynamics, in *Handbook of Atmospheric Electrodynamic*, vol. 2, edited by H. Volland, pp. 249–290, CRC Press, Boca Raton, Fla.

Richmond, A. D. (1995b), Ionospheric electrodynamics using magnetic apex coordinates, *J. Geomagn. Geoelectr.*, *47*, 191–212.

Richmond, A. D., and R. G. Roble (1987), Electrodynamic effects of the thermospheric winds from the NCAR thermospheric general circulation model, *J. Geophys. Res.*, *92*(A11), 12,365–12,376.

Richmond, A. D., and Y. Kamide (1988), Mapping electrodynamic features of the high-latitude ionosphere from localized observations: Technique, *J. Geophys. Res.*, *93*(A6), 5741–5759, doi:10.1029/JA093iA06p05741.

Richmond, A. D., and A. Maute (2014), Ionospheric electrodynamics modeling, in *Modeling the Ionosphere-Thermosphere System*, edited by J. Huba, R. Schunk, and G. Khazanov, John Wiley, Chichester, U. K., doi:10.1002/9781118704417.ch6

Richmond, A. D., S. Matsushita, and J. D. Tarpley (1976), On the production mechanism of electric currents and fields in the ionosphere, *J. Geophys. Res.*, *81*(4), 547–555, doi:10.1029/JA081i004p00547.

Richmond, A. D., E. C. Ridley, and R. G. Roble (1992), A thermosphere/ionosphere general circulation model with coupled electrodynamics, *Geophys. Res. Lett.*, *19*(6), 601–604, doi:10.1029/92GL00401.

Richmond, A. D., C. Peymirat, and R. G. Roble (2003), Long-lasting disturbances in the equatorial ionospheric electric field simulated with a coupled magnetosphere-ionosphere-thermosphere model, *J. Geophys. Res.*, *108*(A3), 1118, doi:10.1029/2002JA009758.

Ridley, A. J., and E. A. Kihn (2004), Polar cap index comparisons with AMIE cross polar cap potential, electric field, and polar cap area, *Geophys. Res. Lett.*, *31*, L07801, doi:10.1029/2003GL019113.

Roble, R. G., and E. C. Ridley (1987), An auroral model for the NCAR thermospheric general circulation model (TGCM), *Ann. Geophys.*, *5A*(6), 369–382.

Roble, R. G., and E. C. Ridley (1994), A thermosphere-ionosphere-mesosphere-electrodynamics general-circulation model (time-GCM): Equinox solar cycle minimum simulations (30–500 km), *Geophys. Res. Lett.*, *21*, 417–420.

Roble, R. G., E. C. Ridley, A. D. Richmond, and R. E. Dickinson (1988), A coupled thermosphere/ionosphere general circulation model, *Geophys. Res. Lett.*, *15*, 1325–1328.

Sabaka, T. J., N. Olsen, and R. A. Langel (2002), A comprehensive model of the quiet-time, near-Earth magnetic field: Phase 3, *Geophys. J. Int.*, *151*, 32–68.

Solomon, S. (2006), Numerical models of the *E*-region ionosphere, *Adv. Space Res.*, *37*, 1031–1037.

Solomon, S. C., and L. Qian (2005), Solar extreme-ultraviolet irradiance for general circulation models, *J. Geophys. Res.*, *110*, A10306, doi:10.1029/2005JA011160.

Stening, R. J. (1971), Longitude and seasonal variations of the *Sq* current system, *Radio Sci.*, *6*, 133–137.

Stening, R. J. (1989), A calculation of ionospheric currents due to semidiurnal antisymmetric tides, *J. Geophys. Res.*, *94*, 1525–1531.

Stening, R. J. (1995), Variations in the strength of the *Sq* current system, *Ann. Geophys.*, *13*, 627–632.

Stening, R. J., and D. E. Winch (2013), The ionospheric *Sq* current system obtained by spherical harmonic analysis, *J. Geophys. Res. Space Physics*, *118*, 1288–1297, doi:10.1002/jgra.50194.

Stening, R. J., J. M. Forbes, M. E. Hagan, and A. D. Richmond (1997), Experiments with a lunar atmospheric tidal model, *J. Geophys. Res.*, *102*(D12), 13465–13471, doi:10.1029/97JD00778.

Sugiura, M. (1964), Hourly values of equatorial *Dst* for the IGY, *Ann. Int. Geophys. Year*, *35*, 9–45.

Suzuki, A. (1978), Geomagnetic *Sq* field at successive universal times, *J. Atmos. Terr. Phys.*, *40*, 449–463.

Suzuki, A. (1979), UT and day-to-day variations in equivalent current systems for world geomagnetic variations, *J. Geomag. Geoelectr.*, *31*, 21–46.

Takeda, M. (1984), Day-to-day variation of equivalent *Sq* current system during March 11–26, 1970, *J. Geomag. Geoelectr.*, *36*, 215–228.

Takeda, M. (1999), Time variation of global geomagnetic *Sq* field in 1964 and 1980, *J. Atmos. Sol. Terr. Phys.*, *61*, 765–774.

Takeda, M. (1991), Role of Hall conductivity in the ionospheric dynamo, *J. Geophys. Res.*, *96*(A6), 9755–9759, doi:10.1029/91JA00667.

Takeda, M. (2002), Features of global geomagnetic *Sq* field from 1980 to 1990, *J. Geophys. Res.*, *107*(A9), 1252, doi:10.1029/2001JA009210.

Takeda, M. (2013), Contribution of wind, conductivity, and geomagnetic main field to the variation in the geomagnetic *Sq* field, *J. Geophys. Res. Space Physics*, *118*, 4516–4522, doi:10.1002/jgra.50386.

Takeda, M., and T. Araki (1985), Electric conductivity of the ionosphere and nocturnal currents, *J. Atmos. Terr. Phys.*, *47*(6), 601–609.

Troshichev, O., V. Andezen, S. Vennerstrom, and E. Friis-Cristensen (1988), Magnetic activity in the polar cap: A new index, *Planet. Space. Sci.*, *36*, 1095–1102.

Troshichev, O. A., R. Y. Lukianova, V. O. Papitashvili, F. J. Rich, and O. Rasumussen (2000), Polar cap index (PC) as a proxy for ionospheric electric field in the near-pole region, *Geophys. Res. Lett.*, *27*(23), 3809–3812.

Vasyliūnas, V. M. (2012), The physical basis of ionospheric electrodynamics, *Ann. Geophys.*, *30*, 357–369.

Wolf, R. A., R. W. Spiro, S. Sazykin, and F. R. Toffoletto (2007), How the Earth's inner magnetosphere works: An evolving picture, *J. Atmos. Sol. Terr. Phys.*, *69*, 288–302, doi:10.1016/j.jastp.2006.07.026.

Xiong, C., H. Lühr, and B. G. Fejer (2016), The response of equatorial electrojet, vertical plasma drift, and thermospheric zonal wind to enhanced solar wind input, *J. Geophys. Res. Space Physics*, *121*, doi:10.1002/2015JA022133, in press.

Xu, W.-Y. (1992), Effects of the magnetospheric currents on the *Sq*-field and a new magnetic index characterizing *Sq* dynamo current intensity, *J. Geomag. Geoelectr.*, *44*, 449–458.

Yamazaki, Y., and M. J. Kosch (2015), The equatorial electrojet during geomagnetic storms and substorms, *J. Geophys. Res. Space Physics*, *120*, 2276–2287, doi:10.1002/2014JA020773.

Yamazaki, Y., A. D. Richmond, H. Liu, K. Yumoto, and Y. Tanaka (2012), *Sq* current system during stratospheric sudden warming events in 2006 and 2009, *J. Geophys. Res.*, *117*, A12313, doi:10.1029/2012JA018116.

Yamazaki, Y., A. D. Richmond, A. Maute, H.-L. Liu, N. Pedatella, and F. Sassi (2014a), On the day-to-day variation of the equatorial electrojet during quiet periods, *J. Geophys. Res. Space Physics*, *119*, 6966–6980, doi:10.1002/2014JA020243.

Yamazaki, Y., A. D. Richmond, A. Maute, Q. Wu, D. A. Ortland, A. Yoshikawa, I. A. Adimula, B. Rabiu, M. Kunitake, and T. Tsugawa (2014b), Ground magnetic effects of the equatorial electrojet simulated by the TIE-GCM driven by TIMED satellite data, *J. Geophys. Res. Space Physics*, *119*, 3150–3161, doi:10.1002/2013JA019487.

Zaka, K. Z., A. T. Kobea, P. Assamoi, K. O. Obrou, V. Doumbia, K. Boka, B. J.-P. Adohi, and N. M. Mene (2009), Latitudinal profile of the ionospheric disturbance dynamo magnetic signature: Comparison with the DP2 magnetic disturbance, *Ann. Geophys.*, *27*, 3523–3536.

Zaka, K. Z., et al. (2010), Simulation of electric field and current during the 11 June 1993 disturbance dynamo event: Comparison with the observations, *J. Geophys. Res.*, *115*, A11307, doi:10.1029/2010JA015417.

Zhang, X., J. M. Forbes, and M. E. Hagan (2010a), Longitudinal variation of tides in the MLT region: 1. Tides driven by tropospheric net radiative heating, *J. Geophys. Res.*, *115*, A06316, doi:10.1029/2009JA014897.

Zhang, X., J. M. Forbes, and M. E. Hagan (2010b), Longitudinal variation of tides in the MLT region: 2. Relative effects of solar radiative and latent heating, *J. Geophys. Res.*, *115*, A06317, doi:10.1029/2009JA014898.

Zhang, Y., and L. J. Paxton (2008), An empirical *Kp*-dependent global auroral model based on TIMED/GUVI FUV data, *J. Atmos. Sol. Terr. Phys.*, *70*, 1231–1242, doi:10.1016/j.jastp.2008.03.008.